Columnar Joints Produced by Cooling in Basalt

Phillips, J.C.[1*], Humphreys, M.C.S.[2†], Daniels, K.A.[1], Brown, R.J.[3‡] & Witham, F.[1§]

[1] Department of Earth Sciences, University of Bristol, Queens' Road, Bristol, BS8 1RJ, UK

[2] Department of Earth Sciences, University of Cambridge, Downing Street, Cambridge, CB2 3EQ, UK

[3] Department of Earth and Environmental Sciences, The Open University, Walton Hall, Milton Keynes, MK7 6AA, UK

Current addresses:

[†] Department of Earth Sciences, University of Oxford, South Parks Road, Oxford, OX1 3AN, UK

[‡] Department of Earth Sciences, Durham University, Science Labs, Durham, DH1 3LE, UK

[§] Rolls-Royce, Gypsy Patch Lane, Bristol, BS34 7QE, UK

Corresponding Author: j.c.phillips@bristol.ac.uk, phone +441179545241, fax +441179253385

ABSTRACT

Columnar jointing in basaltic lava flows on the island of Staffa, NW Scotland, was studied using a combination of field mapping and measurement of column dimensions, sample petrology and measurements of plagioclase crystal size distributions (CSDs) interpreted using theoretical models of cooling. Four different lava flow units were measured, and column ordering was assessed using the hexagonality index and relative standard deviations of column side length, top area and internal angle. Upper and lower colonnades consist of dominantly 5, 6 and 7-sided columns, with a hexagonality index value very similar to that of Giant's Causeway and other basaltic columnar jointed localities. CSDs from samples at different heights within one colonnade were used to infer the propagation of the solidus isotherm, which was consistent with a convective cooling mechanism within the colonnade interior. Sample petrology and CSD measurements suggest that entablature can form both by the interaction of propagating joint sets and flooding of the flow surface by water, and the most widely exposed unit on Staffa shows evidence of both mechanisms operating on the same flow. Crystal size distribution measurements can provide a useful tool for field interpretation of lava flow cooling mechanisms.

KEYWORDS

Columnar jointing, lava flow, basalt, crystal size distribution, convective cooling, fracture pattern

1. INTRODUCTION

Polygonal or columnar jointing is found in lava flows with a range of composition from basalt to rhyolite and formed in a range of environments from subaerial to subglacial, and also in some welded pyroclastic deposits. Many dykes and sills are also columnar-jointed. Similar features are also observed in a wide range of materials including muddy sediments (e.g. Weinberger 1999), permafrost (Lachenbruch 1962) and starch-water mixtures (e.g. Müller 1998a; 1998b). Columnar jointed basalts typically show two jointing facies (Fig. 1): a 'colonnade' comprising regular columns with near-planar sides, and an ‘entablature’ with typically thinner, less regular columns that commonly have curving sides (e.g. Tomkeieff 1940; Spry 1962). Some flows also have an upper colonnade section (Fig. 1b); if present, this is typically of a similar thickness or slightly thinner than the lower colonnade (Long and Wood 1986). The presence of the entablature in the absence of an upper colonnade has been explained by increased rates of cooling caused by flooding of the lava surface, allowing water to access the interior of the flow (Saemundsson 1970). This was based on the fine grain-size, skeletal crystal textures and increased amount of mesostasis (fine-grained groundmass material) in entablature samples compared with those from the colonnade, and was supported by the fact that such lavas were emplaced into palaeo-topographic lows, including river valleys (Swanson 1967; Saemundsson 1970). An alternative to this interpretation, valid for flows with both upper and lower colonnades, is that the entablature represents the region where the two opposing joint sets meet, resulting in a complicated distribution of stress and hence irregular and curving columns (e.g. Xu 1980, reported in Budkewitsch and Robin 1994; Spry 1962). Furthermore, the isotherm velocity (the rate of propagation of a cooling front at a particular temperature) in the centre of a flow is more rapid than at the margins (e.g. Tomkeieff 1940, Grossenbacher and McDuffie 1995), which could result in smaller column diameters. Most recently, Goehring and Morris (2005) observed a discontinuous transition in the scale of jointing in starch-water columnar structures produced at a constant drying rate, and suggested that entablature could form through a similar inherent instability of the system. However, their analogue system differs from cooling lava flows in that joints can only form from the upper surface.

Figure 1 here

Several previous studies have modelled the thermo-mechanical process of joint formation (e.g. Reiter 1987; Degraff and Aydin 1993; Budkewitsch and Robin 1994; Goehring and Morris 2008). Columnar joints are thought to form by spatially-uniform volume contraction during cooling. Stress due to thermal contraction is able to accumulate once the temperature falls below that of elastic behaviour (effectively the glass transition temperature, *Tg,* for typical lava cooling rates), and jointing occurs when the stress exceeds the tensile strength of the material (Budkewitsch and Robin 1994). Thus in a planar layer cooling from above, jointing will propagate progressively downward in increments that roughly follow the passage of the isotherm that defines *Tg*. These joint increments can be observed as *striae* or 'chisel marks' in natural examples of columnar jointed basalt (Fig. 1; Tomkeieff 1940; Ryan and Sammis 1981; Degraff and Aydin 1987). The striae spacing, and thus column diameter, therefore reflect the thermal gradient and cooling rate of the basalt and can be expected to vary with height in a cooling lava flow, dependent on its thermal conditions (e.g. Tomkeieff 1940; Degraff and Aydin 1993; Grossenbacher and McDuffie 1995; Goehring and Morris 2008). Recent field observations and theoretical analysis have shown that constant striae spacing (spacing invariant with height on a given column), as observed at a number of different field localities, is consistent with constant cooling rate controlled by the presence of water inside cooling cracks (Goehring and Morris 2008).

The aim of this study is to investigate in detail the role of the cooling mechanism on columnar jointing patterns, with particular focus on obtaining the best possible constraints from field observations. To do this we conducted a thorough and detailed geological investigation of columnar jointing on the island of Staffa, northwest Scotland, including using field mapping to formally identify different lava flow units, measuring column properties and using petrological methods to estimate emplacement temperatures and cooling rates. Our approach differs from recent studies in that our aim is to infer detailed cooling rate information about individual lava flows and relate these to the observed columnar jointing patterns, rather than to infer global mechanisms from an ensemble of observations from a wide range of field localities with differing emplacement conditions. Our results and observations are complementary to recent studies (e.g. Goehring and Morris 2008) and provide a unique dataset for further interpretative studies.

The paper is set out as follows. In section two, the theoretical background to lava flow cooling is summarised, and the time-dependence of cooling under different mechanisms is identified. In section three, the geological mapping of the island of Staffa and the characteristics of the primary flow units are described; the methodology for the measurement of columnar jointing patterns and petrological analysis of the Staffa lava flows is presented in section four. In section five, corresponding observations and results are presented, with analysis of jointing patterns and calculation of cooling rate described in section six. In sections seven and eight, the implications of the observations and their theoretical interpretation, for mechanisms of formation of columnar jointing patterns, is discussed. Conclusions follow in section nine.

2. THE RELATIONSHIP BETWEEN ISOTHERM PROPAGATION AND COOLING MECHANISM IN A BASALT LAYER

Previous numerical modelling studies have attempted to use the dimensions of basaltic columns (e.g. striae spacing and face widths) to constrain cooling mechanisms. Grossenbacher and McDuffie (1995) showed that a constant ratio of striae spacing to column face width is consistent with purely conductive cooling. More recently, Goehring and Morris (2008) showed that a constant striae spacing, which they observe a few metres below lava flow tops in the Columbia River Basalt, is consistent with a convective cooling regime controlled by water infiltration into the fracture network. The different cooling mechanisms are characterised by different time dependence of isotherm propagation through a lava flow, which can be obtained from one-dimensional models of cooling through a basalt layer. The previous studies have been tested by assuming that pattern ordering depends entirely on the thermal regime, but not with an independent measurement of cooling rate obtained petrologically. Here we use the crystal size distribution of groundmass plagioclase in the basalt to estimate the propagation rate of the solidus isotherm through Staffa lava flows, and compare this with predictions of cooling models that include the latent heat release due to crystallisation.

Following Goehring and Morris (2008), we first consider one-dimensional conductive cooling of a static lava layer from its top only, including the effects of the latent heat release due to crystallisation. This is the classical Stefan problem, which results in a governing equation of the following form,

$$\frac{L\sqrt{\pi}}{c(T_m - T_0)} = \frac{e^{-\lambda^2}}{\lambda \operatorname{erf} \lambda} \quad , \qquad (1)$$

where L is the latent heat of solidification of basalt (taken to be 400 kJ kg^{-1} in this study; Turcotte and Schubert 2002), c is the specific heat capacity of basalt (taken to be 1 kJ kg^{-1} K^{-1} in this study; Turcotte and Schubert 2002), T_m is the initial temperature of the lava flow, T_0 is the ambient temperature and λ is the normalised depth in the flow, defined as

$$\lambda = \frac{z}{2\sqrt{\kappa t}} \qquad (2)$$

where z is the depth below the flow surface, κ is the thermal diffusivity of basalt (taken to be 8 x 10^{-7} m^2 s^{-1} in this study; Watson, 1994) and t is time. Full details of the model formulation are given in Turcotte and Schubert (2002), section 4.18. This model can be solved to predict the vertical position of a given isotherm in the layer as a function of time, and in this study Equation (1) was solved using Newton's method (e.g. Press et al., 1992) which converges rapidly because the right hand side is a monotonic function of λ (Turcotte and Schubert, 2002).

It is also important to consider conductive cooling and solidification from the base of the flow, due to its emplacement onto cold underlying rock. Following Degraff et al (1989), we also solve the Stefan problem for cooling from above and below simultaneously, where the lower layer cooling is described by a solution of similar form to Equation 1. Cooling and solidification from the upper and lower boundaries simultaneously results in a three layer structure, with the molten lava layer in the centre providing an insulating boundary such that cooling in the upper layer is independent of cooling in the lower layer and *vice versa*, because the molten layer temperature remains constant until complete solidification has occurred (Degraff et al 1989). We can thus predict the propagation of the solidus isotherm independently for each layer, and its propagation rate in the upper layer is independent of whether or not there is cooling from below. Stefan approaches have been shown to be in good agreement with measurements at lava lakes (e.g. Turcotte and Schubert 2002), confirming that the density changes due to solidification at the surface do not destabilise the cooling lava layer.

The second model we consider is appropriate for convective cooling, which is envisaged to occur as a result of vaporisation of water that has infiltrated into cracks in the lava flow that are initially formed by conductive cooling (Ryan and Sammis, 1981; Budkewitsch and Robin, 1994). By solving the advection-diffusion equation appropriate to this mechanism of cooling, and comparing with field measurements of striae spacing, Goehring and Morris (2008) show that convective cooling can be characterised by a constant value of the Peclet number,

$$\mathrm{Pe} = \frac{vR}{\kappa}. \tag{3}$$

where v is the solidus isotherm velocity and R is some representative length scale for the fracture pattern, taken to be the area-equivalent cylindrical radius to a hexagonal column of uniform side length. R was also observed to be constant in regions of convective cooling (Goehring and Morris 2008), so linear propagation of the solidus isotherm with time is consistent with a constant Peclet number. Field observations suggest that Pe = 0.3 ± 0.1 (Goehring and Morris, 2008), and in Fig. 2 we show the time-dependence of these model predictions for values of basalt properties appropriate for lava flows on Staffa (see also section six). In accordance with the form of equations (1) and (3), isotherm propagation which shows linear dependence on time is consistent with convective cooling, and non-linear dependence is consistent with conductive cooling.

Figure 2 here

3. THE GEOLOGY OF STAFFA

The island of Staffa is situated off the west coast of the Isle of Mull, northwest Scotland (Fig. 3 inset). The island comprises ~30,000 m^2 with accessible shoreline exposure, and its geology is described by Bailey et al. (1925) and Keay and Keay (1994), with a 1:50,000 map based on the work of Bailey et al. (1925). The island is built from lava flow deposits that form part of the British Tertiary igneous province (Thompson 1982). As part of this study, we re-mapped the geology of the island; the resulting geological map is presented in Fig. 3.

Figure 3 here

The oldest unit outcropping on Staffa is a > 12 m thick basaltic pyroclastic deposit that we interpret to be an ignimbrite, that is exposed around the southern half of the island (Unit 1, Fig. 3). The ignimbrite comprises angular, sub-rounded juvenile scoria and spatter in a poorly sorted lapilli-tuff matrix. Clasts reach up to 1 m in diameter and some exhibit ropey surface textures and cowpat morphologies. Imbricated clasts indicate transport to the southwest. The ignimbrite exhibits a gross normal grading and the upper few metres are weakly stratified. This is overlain by a thick tholeiitic lava with well-developed columnar jointing and entablature zones (Unit 2,

Fig. 3), here called the Fingal's Cave lava flow. The flow is approximately 40 m thick at its maximum (at Fingal's Cave) but thins northwards. Discontinuous lenses of rubbly breccia occur along the base, overlain by coherent columnar-jointed lava, from 1 to >12 m thick, with a vesicular base. This passes abruptly up into an entablature zone that can reach >10 m in thickness and also thins northward. The entablature columns vary from well-formed, curvi-columnar structures in the south to poorly-formed, hackly columns in the north. The lava exhibits a well-defined upper crust, 2-4 m thick, comprising centimetre-thick bands of varying vesicularity. The flow outcrops over much of the southern and northern parts of the island and well-exposed sections occur in the cliffs around Staffa (e.g., Fingal's Cave and Am Buchaille, Fig. 3).

In north-eastern parts of the island (e.g. Meallan Fulann, Fig. 3), Unit 1 is overlain by up to 15 cm of fine- to coarse-grained laminated sediments that may be volcanic ash, and then up to 8 m of a unit that we interpret to be hyaloclastite (Unit 4; Fig. 3); at any rate there is evidence of interaction with external water (see below). The hyaloclastite unit contains large coherent lobes of solid lava up to a few metres thick that may be laterally extensive; large pods or blocks of lava with radiating columns or hackly fractures, and irregular pillow structures indicating interaction with external water (Fig. 4). The joints between pillows sometimes contain fine-grained sediments; laminated sediments were also observed at the base of one of the lava lobes (Fig. 4). The unit is dominated by a rubbly, hackly fractured matrix of small lava fragments, occasionally with sediment filling cracks. One large lobe of coherent lava was sampled for crystal size distribution analysis (see section 4.3).

Unit 4 is overlain by a pinkish-weathered, basaltic lava comprising a vesicular base and a columnar-jointed core up to 7 m thick, in which joints are spaced 50-100 cm apart; a poorly-developed upper crust is present at some locations. The youngest unit outcropping on the island (Unit 6, Fig. 3) is a poorly-exposed columnar-jointed lava visible at the top of cliffs in the northeast of the island. The island is cut by several thin basalt intrusions.

Figure 4 here

Two sample traverses were collected through columnar and entablature basalt. The first profile was taken through a lobe of lava within the hyaloclastite unit on the eastern coast of Staffa (locality 10). The lobe is approximately 5 m thick and the traverse samples the lower colonnade (LC), entablature (ETB) and upper colonnade (UC), and is oriented approximately perpendicular to the contacts between the different jointing zones. The second profile was collected in the lower part of the main Fingal's Cave flow on the west coast of Staffa (locality 8), and samples parts of the lower colonnade and entablature. The jointed basalts were difficult to sample, and most samples were from edges or corners of jointed columns. We note that there could be textural differences between the centres and margins of columns (e.g. Mattson et al. 2011).

4. METHODOLOGY

4.1 Measurement of columnar jointing patterns

At each locality (see Fig. 3), we measured the number of column sides, N, number of neighbouring columns, column side length, L, internal angle between each side, θ, and maximum diameter for each column, D (Figs. 1c and 5). The measurements were made in the field and from digital photographs which were taken vertically above each column top (with a scale bar), with a related sketch for each outcrop (Fig. 6). Where the long axes of columns were exposed, measurements of striae spacing, S, and column side lengths were also obtained to the nearest cm, using a tape measure. The precision of this measurement is conservative, because there was some variation of the striae spacing along the faces of the Staffa columns. A total of 702 column top areas were photographed and measured over eight localities, while >2000 striae spacings and 550 side lengths were measured on 26 columns at three localities.

Figure 5 here

Figure 6 here

Columnar jointing patterns were analysed using two key non-dimensional measures of pattern order. An assessment of pattern maturity was obtained from the Hexagonality Index, χ_N, (Budkewitsch and Robin 1994),

$$\chi_N = \sqrt{(f_5 + f_7) + 4(f_4 + f_8) + 9(f_3 + f_9) + 16 f_{10} + \dots} \quad , \qquad (4)$$

where f_N is the fraction of column tops with N sides. A hexagonality index of zero represents perfectly ordered, hexagonal columns, while $\chi_N = 1$ indicates columns which are all 5- and/or 7-sided and $\chi_N = 2$ indicates columns that are all 4- and/or 8-sided. The degree of regularity of the jointing pattern was also estimated, as in previous studies (e.g. Goehring and Morris 2008) by the relative standard deviation of column side angles, $\sigma(\theta)/\langle\theta\rangle$ (e.g. standard deviation of column side angles divided by the mean side angle). A high relative standard deviation indicates irregular column shapes with a wide variation of internal angles. In contrast, a low (near-zero) value indicates a very regular set of columns. The relative standard deviations of the column top areas ($\sigma(A)/\langle A\rangle$) and side length, ($\sigma(L)/\langle L\rangle$) were also investigated.

4.2. Crystal Size Distributions

Crystal size distributions (CSDs) are now routinely measured in studies of igneous rocks in order to obtain information about the timescales of crystallisation. CSD theory has been described by several authors (e.g. Cashman and Marsh 1988; Cashman 1990; Marsh 1998; Higgins 2002). Processes of stereological correction for converting 2D crystal measurements to true 3D measurements have been developed by Peterson (1996) and Higgins (1994; 2000). The key principle is that, for batch crystallisation of a volcanic rock (which is appropriate for the Staffa case) with crystal population density $n(L)$, where L is grain size, a plot of $\ln(n)$ vs L will normally generate a straight line (the CSD), with gradient $-1/G\tau$ and intercept n_0, where G is the mean growth rate, τ is the residence time of the crystals in the system and n_0 is the nucleation density. This log-linear relationship probably arises because of an exponential increase in nucleation rate with time, with simultaneous steady crystal growth (Marsh 1998). Thus by assuming a value of G, the typical residence time of crystals can be obtained. Because the parameter n_0 is defined per unit volume of magma, a stereological correction must be applied to any 2D measurements of crystal size prior to calculations of the population density.

The two sample traverses were analysed for plagioclase crystal size distributions, with the aim of determining cooling rates for the natural columnar structures. Back-scattered electron images were taken from a polished thin section of each sample. Individual crystals were outlined by hand using the image analysis software package ImageJ (Rasband 1997-2009). The 2D area and Feret length (maximum possible length) were measured, along with the major and minor axes and the orientation of the ellipse best fitting the grain outline. Measurements were calibrated using the scale bar in the SEM image. Approximately 1200-1500 individual grains were measured for each thin section, except for STA10, where only ~430 grains were measured because of weathering. Only whole crystals were measured; crystals only partly in the image were not included in an attempt to minimise edge effects. A few grains that were clearly phenocrysts (having oscillatory or other internal zonation as well as very large crystal size) were ignored, as were some weathered patches, and where possible the total area measured was also corrected for this. Crystals with a Feret length below ~15 μm could not be measured accurately using this technique. To convert the crystal sizes and numbers to 3D populations, the program CSDCorrections 1.3 (Higgins, 2000) was used, assuming negligible preferred orientation. This is reasonable given that values of sample circular variance are $\gtrsim$0.94 for all samples. Crystal shapes were estimated from the mode of intersection length, intersection width and intersection width/length ratios (Higgins 1994). A shape of 1: 4: 12 was used for the hyaloclastite traverse (locality 10), compared with 1: 3: 9 for the West Coast traverse (locality 8). The data were plotted as ln(*n*) *vs* size, where *n* is the 3D population density, using 4-5 logarithmic size intervals per decade (following Higgins 2000).

4.3. Analytical Methods

Back-scattered electron (BSE) images for textural observation and crystal size distribution analysis were taken using a JEOL-JSM-820 scanning electron microscope (SEM) at the University of Cambridge. Representative mineral compositions were obtained using a Cameca 5-spectrometer SX-100 electron microprobe, also at the University of Cambridge. A 2 μm, 15 kV, 10 nA beam was used to analyse major elements, with a 100 nA beam for minor elements (typically K, Cr, Ti and Mn).

5. RESULTS

5.1. Jointing Patterns in Staffa Columnar Basalt

Striae spacings measured on Staffa range from 2-15 cm, with a few wider striae of ~20-25 cm. At any given column, there was a high standard deviation of striae spacings, equivalent to ~30-50% of the average. Average striae spacings were equivalent within these uncertainties for the localities measured. No systematic variation of striae spacing with height in the flow was apparent, although because of the distribution of outcrops, striae spacing and column side lengths could only be measured in restricted parts of the flow. Height in the flow was measured relative to the flow base or entablature boundary. Column side lengths vary widely, from 28-101 cm, with two measurements at 145 cm (from locality 5). As with the striae spacing, there is no consistent systematic variation of column side length with height in the flow. At any given locality, the side lengths of individual columns can remain constant with height. Occasionally, step changes in side length of a given column are observed at column terminations. The average striae spacing measured for each column is proportional to the average face width (Fig. 7); striae spacings are 7-20% of the face width at Staffa. This is consistent with observations from the Columbia River basalt and other similar flows, and corroborates the findings of previous studies (Degraff and Aydin 1987; Grossenbacher and McDuffie 1995; Goehring and Morris 2008) in suggesting underlying control by the mechanical properties of the rock (Young's Modulus and Poisson's ratio).

Figure 7 here

Column side lengths and column top areas are significantly smaller in the entablature compared with the colonnade (table 1). For example, in the entablature at locality 7, the average side length is only 12 cm, in comparison with 40 cm in the colonnade at locality 2. The transition between entablature and colonnade is typically sharp. At locality 4 the average side length in the colonnade is 36 cm. This decreases abruptly to 12 cm in the entablature, over a height of only 2 metres. At locality 4, average side lengths and column top areas were measured as a function of distance above the colonnade–entablature transition. Column side lengths show little variation with height over the observed range.

The maturity of columnar jointing patterns on Staffa was assessed using the hexagonality index (χ_N) and the relative standard deviation of column geometry as measures of order. For the colonnade localities χ_N is low, 0.79 – 0.87 (with one locality at 0.93), with <N> of 5.7-6.1, reflecting mature joint patterns dominated by 5-, 6- and 7-sided columns (Table 1; Fig. 8). The dominant column shape is 6-sided. The two entablature localities have differing hexagonality index values. Locality 4 has a low χ_N of 0.82 and <N> of 5.9, similar to that of the colonnade localities. Locality 7 has a higher χ_N of 1.20 with <N> of 5.3, indicating a crack pattern containing abundant 4-, 5-, 6- and 7-sided columns, and dominated by 5-sided columns (table 1). The lava lobe within the hyaloclastite unit at locality 10 also gave a high χ_N value of 1.11 with <N> of 5.5 (Table 1). For comparison, joint patterns at the Giant's Causeway, Northern Ireland give χ_N of 0.78 and 0.80 (Beard 1959; data from O'Reilly, 1879), very similar to that for Staffa. Other datasets for jointed basalt give χ_N 0.92 and 1.06 (Devil's Postpile, California and Mount Rodeix, Auvergne respectively; Beard 1959).

Figure 8 here

Table 1 here

The relative standard deviation of internal angles, $\sigma(\theta)/\langle\theta\rangle$, is low for all localities (Fig. 8). Hexagonality correlates positively with $\sigma(\theta)/\langle\theta\rangle$, which is unsurprising because columns with more sides must have a higher average internal angle, since the sum of the external angles of a polygon is 360°. Thus patterns that have high hexagonality index (i.e. a higher relative abundance of 3-, 4-, 5-, 7- and 8-sided columns) will have a greater spread of internal angles. The colonnade localities give $\sigma(\theta)/\langle\theta\rangle$ of 0.15 – 0.19, indicating a relatively low spread of column angles around the mean. The entablature localities have slightly higher $\sigma(\theta)/\langle\theta\rangle$ of 0.16 (locality 4) and 0.23 (locality 7), indicating a slightly wider spread of angles, at least for locality 7. For comparison, the Giant's Causeway has $\sigma(\theta)/\langle\theta\rangle = 0.13$, slightly lower than the Staffa colonnade localities.

There is little difference in relative standard deviation of column side length, ($\sigma(L)/<L>$), between the colonnade and entablature samples. All localities gave similar values, 0.42 – 0.52 (Table 1; Fig. 8). However, the relative standard deviation of column top area, $\sigma(A)/<A>$, shows a clear contrast between facies, reflecting the general decrease in column dimensions in the entablature. Hexagonality index correlates positively with both $\sigma(A)/<A>$, which results from the tendency for columns with more sides to have a greater maximum diameter, and $<A>$ (e.g. Rivier and Lissowski 1982). The colonnade localities have low $\sigma(A)/<A>$, 0.35 – 0.58, whereas the entablature localities give higher values of 0.57 (locality 7) and 0.66 (locality 4). These data indicate that entablature columns are slightly more variable in shape and size, as well as being smaller than those of the colonnade. The Giant's Causeway data give $\sigma(A)/<A> = 0.34$, again slightly lower than the Staffa colonnade samples (Fig. 8).

Average values for the lava lobe within the hyaloclastite unit are similar to those from the entablature (Table 1; Fig. 8). Although relatively few column dimensions could be measured, and no striae were observed, average side length is clearly greater in the upper and lower colonnade structures, and smaller in the central entablature zone.

5.2. Crystal Size Distributions

Two sample profiles were analysed: a profile through part of the Fingal's Cave lava colonnade at locality 8, and a profile through the lava lobe at locality 10 (Fig. 3). The West Coast (Fingal's Cave) samples typically show a linear CSD, with a down-turn at crystal lengths below ~ 100 μm (true crystal size), which equates to a measured Feret length of < 40 μm. This is probably related both to difficulty in measuring the smallest grains, and a true deficiency of crystals in the smallest size ranges due to growth. Fits to the straight parts of the CSDs are very good, with $R^2 > 0.995$. The gradient is similar throughout the Lower Colonnade, but lower for the entablature (Fig. 9). As the gradient is equivalent to $1/G\tau$ this suggests either a longer crystallisation time (τ) or higher growth rate (G) for the entablature. The intercept is also slightly higher in the entablature.

Figure 9

The samples from the lava lobe within the hyaloclastite unit also show linear CSDs (Fig. 9), with a sharp down-turn at lengths below ~60 μm (true crystal size, or < 25 μm Feret diameter). Fits to the straight parts of the CSD are again very good, with $R^2 > 0.993$. There is no systematic difference in gradient or intercept between the samples in this traverse. Gradients are in the range -0.0238 μm^{-1} to -0.0191 μm^{-1} (Table 2).

Table 2 here

5.3. Sample Petrology

Several of the samples show signs of alteration, which mainly affects olivine and glass. The basalts contain sparse phenocrysts of plagioclase + clinopyroxene + olivine (typically altered), with a coarse-grained groundmass of randomly oriented, tabular plagioclase, clusters of granular pyroxene, olivine, and oxides of varying morphology. Clinopyroxene phenocrysts commonly contain lath-shaped inclusions of plagioclase in their cores. Plagioclase, clinopyroxene and olivine crystals show strong compositional zoning at their margins.

In the samples from the lava lobe within the hyaloclastite unit, planar-sided patches of groundmass between plagioclase grains are extensive and show evidence of silicate liquid immiscibility in the form of quenched droplets of dark, probably Fe-rich material (Fig. 10). No analyses could be obtained owing to the small size of the droplets; however they are interpreted as Fe-rich and Si-rich droplets on the basis of previous studies (e.g. Roedder and Weiblen 1970; Philpotts, 1979; Jakobsen et al. 2005; Charlier and Grove 2012). The droplets appear to be most fine-grained in the entablature section of this unit.

Figure 10 here

The morphology of the oxides grains varies both within and between the traverses. In the thin lava lobe within the hyaloclastite unit, all the oxides are cruciform to dendritic (Fig. 10); however the oxides in samples from the entablature are finer and more delicate in structure than those in the columnar sections. In the West Coast traverse, oxides are tabular and subophitic in lower (columnar) parts (e.g. STA7). They become less tabular, more elongate, and even hopper-shaped with height (e.g. STA9), while the entablature contains dendritic forms (STA10).

5.4. Mineral Compositions

Groundmass plagioclase has calcic cores (An_{73}-An_{89}) with overgrowth rims that are strongly and progressively zoned to oligoclase-anorthoclase. The plagioclase contains up to 1.41 wt% FeO, 0.35 wt% MgO and 0.18 wt% TiO_2 (Fig. 11). Kinks in minor element concentrations with decreasing X_{An} probably indicate fractionation of olivine ± pyroxenes followed by Fe-Ti oxides (Fig. 11), and thus confirm that plagioclase was crystallising throughout the cooling time of the lava flow. Clinopyroxene is augitic, with Mg# 80-57. Core and rim compositions of clinopyroxenes overlap, but the rims extend to more evolved compositions with lower Mg#, lower Cr_2O_3, higher TiO_2 and higher Na_2O. Opaque minerals are mainly ilmenite and titanomagnetite. The titanomagnetite has variable TiO_2 content (65-95 mol% Usp), suggesting crystallisation over a wide range of temperatures and/or a range of fO_2 conditions. Temperature estimates were obtained from coexisting ilmenite-titanomagnetite pairs in the Fingal's Cave lava, with oxide formulae calculated according to Stormer (1983), and using QUILF (Andersen et al. 1993). These gave temperatures of 968-1007 °C and log fO_2 -10.8 to -11.6 (0.0 to 0.2 log units above the FMQ buffer).

Figure 11 here

6. ANALYSIS

6.1. Use of Crystal Size Distributions to Constrain Cooling Rates for Staffa Basalts

Our approach is essentially to assume that plagioclase crystallisation occurs throughout the liquidus-solidus temperature interval, and to estimate the residence time for plagioclase using CSDs, to give an average cooling rate over that interval. In detail, we assume that the lava is emplaced at its liquidus, which is estimated to be ~1145 to 1190°C, based on MELTS estimates (Ghiorso and Sack 1995) using bulk compositions of Staffa Magma Type lavas given by Thompson et al. (1986). This range of liquidus temperatures is also consistent with experimentally-determined liquidus temperatures for the Rattlesnake Hill basalt (1150-1180°C, Philpotts 1979) which shares many of the textural and chemical features of the Fingal's Cave lava. The solidus temperature is approximately 950°C, based on experimental observations (Philpotts 1979). Thus the crystallisation interval is approximately 200-240°C, and we assume that plagioclase crystallises throughout this interval. Plagioclase phenocrysts are essentially absent, indicating that plagioclase did not start to grow before emplacement of the flow. The residence time for plagioclase, obtained using CSDs, therefore gives us the time for the lava flow to cool between 1170°C and 950°C. We recognise that this simplification could include some cooling time while the flow was being emplaced, but we consider this to be small relative to the total cooling time. By determining this cooling time for different sampling positions through the lava, the propagation of the 950°C isotherm can be tracked. We recognise that there may be textural differences in crystal size distribution between the margins and centres of basaltic columns (Mattson et al. 2011) but we were not able to control for this in our sampling, except that column cores were not sampled. However, all our sample profiles were collected in the same way, and the uncertainties associated with the sampling are probably small relative to uncertainties in crystal growth rates, for example.

In order to use the CSD to estimate the solidus isotherm propagation for a particular sampling position, an estimate of the crystal growth rate is required, which is unconstrained by the sample properties (see section 3.3). However, estimates of plagioclase growth rates in basaltic dykes and flows have been reasonably well constrained in previous petrological studies. These estimates range from 1.3×10^{-6} mm/s for dykes 30-50 cm thick (Ikeda 1977, reported in Cashman 1990) to 1.3×10^{-9} to 9.0×10^{-9} mm/s for dykes 15-30 m thick (Ikeda 1977; Kneedler 1989; reported in Cashman 1990). In comparison, crystallisation rates for surface lavas range from 1×10^{-9} to 6×10^{-10} mm/s (Makaopuhi lava lake, Cashman and Marsh 1988) and 2×10^{-6} to 4×10^{-9} mm/s (Mauna Loa, Cashman 1990), to 1.7×10^{-7} to 1.3×10^{-8} mm/s for Kilauea lavas (Burkhard 2002). We therefore assumed growth rates of 10^{-8} to 10^{-9} mm/s as most representative of the likely crystallisation conditions. Fig. 12 shows isotherm propagation trends for crystal growth rates of 10^{-9} and 10^{-8} mm s^{-1}, for the Fingal's Cave lava flow sample traverse at locality 8, where this flow has a thickness of about 12 m.

Figure 10 here

Fig. 12 suggests that the 950°C isotherm propagates linearly with time through the interior of the flow (within the range of sample positions). The cooling time to 950 °C for the flow interior, calculated using $G = 10^{-9}$ mm s^{-1}, has a comparable magnitude to previous estimates and observations of basalt cooling times (e.g. Cashman 1990; Turcotte and Schubert 2002) which suggest times of 12-20 months at depths of about 8 metres below the flow top. However, the isotherm propagation time trend should reach zero time at the upper margin of the flow. If we use the higher crystal growth rate (10^{-8} mm s^{-1}) we calculate isotherm propagation times that are much shorter (indicating much more rapid cooling) for the flow interior, which is inconsistent with previous observations as outlined above. This reveals a clear inconsistency in our use of the same value of G near the flow margin, because the isotherm propagation time trend for the flow interior cannot be extrapolated to match cooling conditions in the flow margin (Fig. 12). The only reasonable conclusion is that crystal growth rates are significantly higher near the flow margin compared to the interior. The effect of this would be to change the gradient of the isotherm propagation time in this region; much closer sampling would be required to test this hypothesis.

Irrespective of the details of the cooling trends near the flow margin, our data clearly show a linear isotherm propagation rate with depth in the flow (Fig. 12). We cannot fit the alternative curved trend (cf Fig. 2) to the data for any reasonable physical conditions (temperature contrasts, latent and specific heats of basalt). From our comparison of field measurements of the solidus isotherm propagation with one-dimensional cooling models (Fig. 2), we therefore infer that convective cooling is the dominant mechanism for the Fingal's Cave lava at locality 8, combined with strong conductive cooling at the flow top itself. We found the ratio of striae spacing to face width to be in accord with measurements at other basalt flows (Goehring and Morris 2008), and found little variation in their absolute values within the colonnades sampled, within the uncertainty of our measurements. Constant striae spacing has been shown to be consistent with convective cooling of the basalt due to the presence of water within fractures (Goehring and Morris 2008) and therefore supports our interpretations based on isotherm propagation rates. This result for Staffa is consistent with those of Goehring and Morris (2008) for the Columbia River Basalt flows, which also suggest a convective cooling mechanism within the interior of the flow.

7. EVOLUTION AND MATURITY OF NATURAL JOINTING PATTERNS

We have used the hexagonality index, χ_N, as a measure of the maturity of a jointing pattern, following Budkewitsch and Robin (1994). The most mature patterns show relatively low values of χ_N, including those in the Fingal's cave colonnade (Fig. 8; table 1) and at Giant's Causeway (Beard 1959); the most mature jointing patterns are commonly agreed to have formed in the most slowly cooled lavas. However, the apparent strong variations in growth rate at the flow top (inferred above) raise a key question. These jointing patterns must have been initiated under very rapid cooling conditions: how do they achieve their very mature flow centres? Gray et al. (1976) argued that such mature patterns (with Y-shaped crack terminations, i.e. internal angles approaching 120°) could not nucleate by simple fracturing in a plane, but must result from maturation of an initial joint pattern, by selective propagation of certain joint orientations. Pattern coarsening is therefore achieved by termination of certain joints and rearrangement of the neighbouring columns (Budkewitsch and Robin 1994; Jagla 2004; Goehring and Morris 2005).

Jagla (2004) carried out numerical simulations of jointing patterns for a range of stages in the temporal evolution of a contracting elastic sheet. Evolution of the crack pattern occurred spontaneously in order to reduce the mechanical energy of the pattern (Jagla 2004). We digitised the resulting patterns (Jagla 2004, Fig. 2b-d) and the data show a positive correlation between $\sigma(A)/\langle A\rangle$ and χ_N, with the more mature patterns giving lower χ_N (Fig. 8). In the numerical simulations pattern maturation occurred by increasing the regularity of polygon cross-sections by crack termination and merging smaller columns with fewer sides (Jagla 2004), resulting in decreased χ_N and decreased column area variability ($\sigma(A)/\langle A\rangle$). The basalt joint patterns measured on Staffa approach the most mature numerical pattern (Fig. 8), but although the use of several localities exposed through erosion has given a spread of statistical data, it is clearly difficult to image serial sections through the joint patterns in a lava flow. We therefore suggest that the initial jointing pattern at the flow top on Staffa may have been similar to those observed at lava lakes, where the hot lava surface is in contact with air (or water). This is supported by data from lava lakes, digitized from Peck and Minakami (1968), which give high χ_N (0.77-1.0), low numbers of sides <N> and high column area variability (σ(A)/<A>, table 1, Fig. 8). Overall, the average number of column faces, <N>, also increases as χ_N decreases for basalt. We suggest that an initial jointing pattern with similar statistical variability to the lava lakes nucleated at the surface of the Staffa flow and propagated downward, rapidly become more mature by selective joint termination and merging of adjacent columns.

Hexagonality can also vary independently of <N> or relative standard deviations of column dimensions. Fig. 8 also shows different mature statistical distributions of 2D polygons, including one based on a Poisson distribution (Crain 1978), and two close packing arrangements developed for division of territory within bird species (Tanemura and Hasegawa 1980). In all three the average number of column sides is 6.00 (Budkewitsch and Robin 1994). The Poisson distribution has $\chi_N = 1.33$, while the random close packing model has $\chi_N = 0.80$ and the regular close packing model $\chi_N = 0.54$ (Fig. 8). The basalt columns show similar χ_N to these mature theoretical distributions (Fig. 8), with slightly higher χ_N for the entablature, consistent with a higher cooling rate and less mature jointing pattern. However, the basaltic jointing patterns overlap most closely with the theoretical random close packing arrangement (Fig. 8). In previous models of joint propagation (e.g. Ryan and Sammis 1981; Degraff and Aydin 1993; Lachenbruch 1962), lateral joint spacing (*i.e.* column diameter) is controlled by the distance over which tensile stress can be relieved by the formation of a new *stria*. Wider joint segments relieve stress over a greater area, leading to increased joint spacing. The 'hard centres' of the random close-packed circles are therefore analogous to the regions over which tensile stress is relieved by cracking and thus may have some physical meaning for the thermal joint patterns. Hexagonality index will decrease to zero for a perfectly regular hexagonal arrangement of columns, but the smallest value observed for the Fingal's Cave lava is approximately 0.80, indicating that even the most regular basaltic columns have some inherent variability (Goehring and Morris 2008).

8. ORIGIN OF ENTABLATURE AND COLONNADE STRUCTURES ON STAFFA

The origin of basaltic entablature has previously been ascribed to flooding of the flow surface with water (Saemundsson 1970; Long and Wood 1986), interaction between propagating joint sets (Xu 1980; Spry 1962) and to intrinsic discontinuities in pattern scaling (Goehring and Morris 2005). The occurrences of columnar jointing on Staffa probably reflect more than one mode of entablature formation. For example, the lava lobe at locality 10 shows clear upper and lower columnar layers, while the centre of the lobe is an irregular, hackly entablature (see Fig. 4). The average side length of the columns decreases smoothly upward into the entablature, and can be seen to increase across the entablature-upper colonnade boundary. There is no clear textural difference between entablature and colonnade samples from the lava lobe in the hyaloclastite unit, and their CSDs are equivalent. This indicates no strong change in cooling rate at the entablature, and suggests that the entablature represents an interaction between two converging joint sets.

In contrast, the Fingal's Cave lava has no upper colonnade exposed, but a very thick entablature (several metres at Fingal's Cave itself) which thins northward. Column dimensions in the colonnade are consistent across the flow. At Fingal's Cave there is an abrupt change in lengthscale and pattern maturity at the colonnade – entablature boundary, accompanied by a clear change in rock texture to finer grainsize and dendritic oxides. This suggests rapid quenching, probably by ingress of surface water into the joints (Long and Wood 1986; Lyle 2000). This is supported by the cooling rate calculations presented in this study, which indicate convective cooling (see earlier). On the north coast of Staffa, the Fingal's Cave flow is much thinner, as is the entablature, which grades upwards into an upper colonnade. Furthermore, while the entablature at Fingal's Cave is strongly curvi-columnar with clearly continuous columns, on the north coast the columns are less well-defined. Separating the two localities is a sizeable exposure of hyaloclastite breccia that outcrops in the northeast of the island (see Fig. 3). We therefore suggest that part of the Fingal's Cave flow was emplaced into a lake or similar feature, resulting in surface flooding and water ingress along joints, and hence the rapidly quenched entablature in the south of the island. The northern parts of the flow were probably not erupted into water; the entablature here may reflect the interaction of propagating joint sets from the upper and lower colonnade. Thus entablature jointing can form through different mechanisms, even within a single flow.

9. CONCLUSIONS

We have studied columnar jointing in basaltic lava flows on the island of Staffa, using a combination of field mapping and measurement of column dimensions, sample petrology and plagioclase crystal size distributions (CSDs) coupled with theoretical constraints to identify the dominant cooling mechanism. The main conclusions from this study are as follows:

1. There are four different lava flow units on the island of Staffa, which provide a range of exposure of columnar jointing at both column tops and column sides. Basaltic colonnades consist of dominantly 5, 6 and 7-sided columns, with a hexagonality index value very similar to that of Giant's Causeway and other basaltic columnar jointed localities.

2. There is no systematic variation of striae spacing or column face width within the colonnades, which is consistent with observations at other field areas, and has been previously interpreted as consistent with convective cooling of the interior of the lava flow by water.

3. The column side lengths and top areas are significantly smaller in the lava flow entablature compared with the colonnades. Two entablature localities studied in detail show widely different values of hexagonality index, one similar to the colonnade values and the other indicating abundant 4, 5, 6, 7 -sided columns, with similar hexagonality index values to a nearby hyaloclastite lava flow unit.

4. The hexagonality index provides a useful measure of maturity (i.e. tendency of columns to be six-sided) for natural columnar jointing patterns. Trends in hexagonality index are consistent with those of other commonly-used measures such as relative standard deviation of column top area, face width and internal angle.

5. The initial jointing pattern that formed on the flow surface at Staffa was probably immature, with high χ_N and variable column dimensions, perhaps similar to the patterns observed at lava lakes. As the jointing pattern propagated down into the flow interior, it matured by selective joint termination and merging of columns. The mature pattern has similar statistical variability to a random close packing of hard spheres.

6. Crystal size distributions from samples at different heights within one colonnade were used to infer the propagation of the solidus isotherm. When compared with the predictions of one-dimensional theoretical models, this suggested that the isotherm propagation was consistent with a convective cooling mechanism within the colonnade interior, supporting the lack of systematic variation in striae spacing or face width. Conductive cooling models cannot fit the isotherm propagation data. A distinctly different cooling mechanism must have operated close to the margin, which is inconsistent with convective cooling for any range of Peclet numbers that are considered reasonable for basaltic lava flows.

7. Sample petrology and CSD measurements suggest that the entablature can form from both the interaction of propagating joint sets and from flooding of the flow surface by water, and the most widely exposed unit on Staffa shows evidence of both mechanisms operating on the same flow.

8. Crystal size distributions, coupled with one-dimensional numerical models, can provide a useful tool for field interpretation of lava flow cooling mechanisms, but more work is needed to find robust independent methods for determining crystal growth rates.

ACKNOWLEDGEMENTS

We gratefully acknowledge a grant from the Edinburgh Geological Society which contributed towards fieldwork costs. We thank Chiara Petrone for assistance with electron microprobe analyses, Bob Mehew for helpful discussions and photographs, Thierry Menand for useful discussions about fracturing, and Scottish Natural Heritage for permission to work on the island. MCSH was supported by a Junior Research Fellowship from Trinity College, Cambridge.

REFERENCES

Andersen DJ, Lindsley DH, Davidson PM (1993) QUILF: A Pascal program to assess equilibria among Fe-Mg-Ti oxides, pyroxenes, olivine and quartz. Computers and Geosciences 19:1333-1350

Bailey EB, Anderson EM, Burnett GA, Richey JE, Lee GW, Wright WB, Wilson GV, Thomas HH (1925) The geology of Staffa, Iona and western Mull. *Memoirs of the Geological Survey of Scotland*

Beard CN (1959) Quantitative study of columnar jointing. Geological Survey of America Bulletin 70:379-382

Budkewitsch P, Robin P-Y (1994) Modelling the evolution of columnar joints. Journal of Volcanology and Geothermal Research 59:219-239

Burkhard DJM (2002) Kinetics of crystallization: example of micro-crystallization in basalt lava. Contributions to Mineralogy and Petrology 142:724-737

Cashman KV (1990) Textural constraints on the kinetics of crystallization of igneous rocks. Reviews in Mineralogy 24:259-314

Cashman KV, Marsh BD (1988) Crystal size distribution (CSD) in rocks and the kinetics and dynamics of crystallization II: Makaopuhi lava lake.

Charlier B, Grove TL (2012) Experiments on liquid immiscibility along tholeiitic liquid lines of descent. Contributions to Mineralogy and Petrology (in press), doi: 10.1007/s00410-012-0723-y

Crain IK (1978) The Monte-Carlo generation of random polygons. Computers and Geosciences 4:131-141

Degraff JM, Aydin AA (1987) Surface morphology of columnar joints and its significance to mechanics and direction of joint growth. Geological Society of America Bulletin 99: 605-617

Degraff JM, Aydin AA (1993) Effect of thermal regime on growth increment and spacing of contraction joints in basaltic lava. Journal of Geophysical Research 98: 6411-6430

Degraff JM, Long PE, Aydin AA (1989) Use of joint-growth directions and rock textures to infer thermal regimes during solidification of basaltic lava flows. Journal of Volcanology and Geothermal Research 38:309-324

Ghiorso MS, Sack RO (1995) Chemical mass transfer in magmatic processes. IV. A revised and internally consistent thermodynamic model for the interpolation and extrapolation of liquid-solid equilibria in magmatic systems at elevated temperatures and pressures. Contributions to Mineralogy and Petrology 119:197-212

Goehring L, Morris SW (2005) Order and disorder in columnar joints. Europhysics Letters 69:739-745

Goehring L, Morris SW (2008) Scaling of columnar joints in basalt. Journal of Geophysical Research 113:B10203

Gray NH, Anderson JB, Devine JD, Kwasnik JM (1976) Topological properties of random crack networks. Mathematical Geology 8:617-626

Grossenbacher KA, McDuffie SM (1995) Conductive cooling of lava: columnar joint diameter and stria width as functions of cooling rate and thermal gradient. Journal of Volcanology and Geothermal Research 69:95-103

Higgins MD (1994) Numerical modelling of crystal shapes in thin sections: Estimation of crystal habit and true size. American Mineralogist 79:113-119

Higgins MD (2000) Measurements of crystal size distributions. American Mineralogist 85:1105-1116

Jagla EA (2004) Maturation of crack patterns. Physical Review E 69:056212

Jakobsen JK, Veksler IV, Tegner C, Brooks CK (2005) Immiscible iron- and silica-rich melts in basalt petrogenesis documented in the Skaergaard intrusion. Geology 33:885-888

Keay J, Keay J (1994) Collins Encyclopaedia of Scotland. Harper Collins Publishers, London

Lachenbruch AH (1962) Mechanics of thermal contraction cracks and ice-wedge polygons in permafrost. *Special Paper of the Geological Society of America* **70**, 69pp

Long PE, Wood BJ (1986) Structures, textures and cooling histories of Columbia River basalt flows. Geological Society of America Bulletin 97:1144-1155

Lyle P (2000) The eruption environment of multi-tiered columnar basalt lava flows. Journal of the Geological Society, London 157:715-722

Marsh BD (1998) On the interpretation of crystal size distributions in magmatic systems. Journal of Petrology 39:553-599

Mattson HB, Caricchi L, Almqvist BSG, Caddick MJ, Bosshard SA, Hetenyi G, Hirt A.M. (2011) Melt migration in basalt columns driven by crystallization-induced pressure gradients. Nature Communications 2:299 doi: 10.1038/ncomms1298

Müller G (1998a) Experimental simulation of basalt columns. Journal of Volcanology and Geothermal Research 86:93-96

Müller G (1998b) Starch columns: Analog model for basalt columns. Journal of Geophysical Research 103:15239-15253

O'Reilly JP (1879) Explanatory notes and discussion on the nature of the prismatic forms of a group of columnar basalts, Giant's Causeway. Transactions of the Royal Irish Academy 26:641-728

Peck DL, Minakami T (1968) The formation of columnar joints in the upper part of Kilauean lava lakes, Hawaii. Geological Society of America Bulletin 79:1151-1116

Peterson TD (1996) A refined technique for measuring crystal size distributions in thin section. Contributions to Mineralogy and Petrology 124: 395-405

Philpotts AR (1979) Silicate liquid immiscibility in tholeiitic basalts. Journal of Petrology 20:99-118

Press WH, Flannery BP, Teukolsky SA, Vetterling WT (1992) Numerical Recipes. Cambridge University Press

Rasband WS (1997-2009) ImageJ. U.S. National Institutes of Health, Bethesda, MD. http://rsb.info.nih.gov/ij. Accessed 28 June 2008

Rieter M, Barroll MW, Minier J, Clarkson G (1987) Thermo-mechanical model for incremental fracturing in lava flows. Tectonophysics 142:241-262

Rivier N, Lissowski A (1982) On the correlation between sizes and shapes of cells in epithelial mosaics. Journal of Physics A: Mathematical and General 15: L143-L148

Roedder E, Weiblen PW (1970) Silicate liquid immiscibility in lunar magmas, evidenced by melt inclusions in lunar rocks. Science 167:641-644

Ryan MP, Sammis CG (1981) The glass transition in basalt. Journal of Geophysical Research 86:9519-9535

Saemundsson K (1970) Interglacial lava flows in the lowlands of southern Iceland and the problem of two-tiered columnar jointing. Jokull 20:62-77

Spry A (1962) The origin of columnar jointing, particularly in basalt flows. Australian Journal of Earth Sciences 8:191-216

Stormer JC (1983) The effects of recalculation on estimates of temperature and oxygen fugacity from analyses of multi-component iron-titanium oxides. American Mineralogist 66:586-594

Swanson DA (1967) Yakima basalt of the Tieton River area, south central Washington. Geological Survey of America Bulletin 78:1077-1110

Tanemura M, Hasegawa M (1980) Geometrical models of territory. 1. Models for synchronous and asynchronous settlement of territories. Journal of Theoretical Biology 82:477-496

Thompson RN (1982) Magmatism of the British Tertiary Volcanic Province. Scottish Journal of Geology 18:49-107

Thompson RN, Morrison MA, Dickin AP, Gibson IL, Harmon RS (1986) Two contrasting styles of interaction between basic magmas and continental crust in the British Tertiary Volcanic Province. Journal of Geophysical Research 91:5985-5997

Tomkeieff SI (1940) The basalt lavas of the Giant's Causeway district of Northern Ireland. Bulletin of Volcanology 6:89-143

Turcotte DL, Schubert G (2002) Geodynamics. 2^{nd} Ed. Cambridge University Press

Watson EB (1994) Diffusion in volatile-bearing magmas in Carroll, M.R. & Holloway, J.R. (eds) Volatiles in Magmas. Min. Soc. Am. Rev. Min. 30:371-411

Weinberger R (1999) Initiation and growth of cracks during desiccation of stratified muddy sediments. Journal of Structural Geology 21:379-386

Xu S (1980) Discussion on the morphological charactersistics of two-layer columnar joints in basalt and their forming mechanism. Geological Review (in Chinese, with English abstract), 26:510-515

FIGURE AND TABLE CAPTIONS

Fig. 1

Schematic columnar jointing architecture. (a) and (b) Possible relationships between entablature and colonnade; (c) Measurable dimensions of an individual column include the diameter (D), side length (L), striae spacing or width (S) and the internal angles (θ).

Fig. 2

Theoretical predictions of the time to cool to 950°C for a 10 m thick basalt layer initially emplaced at 1170°C. The solid lines show the case of conductive cooling and solidification (Stefan solutions), and the dashed lines show the case of convective cooling due to vapourisation of water for Peclet numbers of 0.3 (dashed line) and 0.4 (dotted line). Convective cooling is consistent with propagation of the solidus isotherm that is linear with time.

Fig. 3

Geological map (right) and stratigraphic section (left) for Staffa. Inset shows location of the Isle of Mull (shaded) with arrow to indicate the location of the island of Staffa. Localities studied are marked with large dots and a locality number (small dots indicate topographic spot heights).

Fig. 4

Field relationships within Unit 4, interpreted as hyaloclastite. (a) Lobe of lava (right) with well-developed columns (colonnade, C) at base and hackly entablature (ETB) in upper part (upper colonnade not seen in this view). The lava is underlain by bedded sediments (S) of variable grainsize. Lava pod with radiating cracks is seen to upper left on the far side of a steeply dipping fault. (b) Pillow-like structures in the same unit; narrow bands of sediment separate some pillows (arrowed). (c) Cherty sediment between pillow structures.

Fig. 5

Field examples of jointing from Staffa. (a) The Fingal's Cave flow at its thickest point showing upper entablature, lower colonnade and underlying ignimbrite; (b) Typical column faces with sub-horizontal *striae*; (c) View of column tops in the entablature, Staffa, showing 4- to 6-sided, polygonal columns.

Fig. 6

Examples of typical entablature (top, locality 7) and colonnade (bottom, locality 1) flow tops measured for statistical parameters. Each increment on the scale bar represents 10 cm.

Fig. 7

Width of joint increments (striae widths, S) follows a rough proportionality with column side lengths (L) for Staffa (black diamonds), in agreement with previously published data from other column jointed basalt localities (Boiling Pots, Hawaii, Ryan and Sammis 1978; First Watchung, New Jersey, USA, Ryan and Sammis 1978; Prehistoric Makaopuhi lavas, Hawaii, Ryan and Sammis 1978; and Columbia River basalts, USA (Grossenbacher and McDuffie 1995; Goehring and Morris 2008). Contours represent lines of constant S/L.

Fig. 8

Column top measurements from experimental and natural jointing patterns. Hexagonality index (χ_N) *vs* (a) average number of sides, <N>; (b) relative standard deviation of column side lengths, σ(L)/<L>; (c) relative standard deviation of column top areas, σ(A)/<A>; (d) relative standard deviation of column internal angles, σ(θ)/< θ >. Red squares: entablature and hyaloclastite (H) jointing patterns from Staffa. Triangles: measurements from other columnar jointed basalt localities, including Mount Rodeix (MR), Auvergne, Devil's Postpile (DP), California, and the Giant's Causeway (GC), Ireland. Data for MR and DP taken from Budkewitsch and Robin (1994); data for GC from Beard (1959) and digitised from O'Reilly (1879). Black dots: numerically simulated distributions from (1) Crain, 1978; (2) Random close packing model, Tanemura and Hasegawa, 1980, reported in Budkewtisch and Robin (1994); (3) Regular close packing model digitised from Tanemura and Hasegawa (1980). Un-numbered dots are progressively maturing patterns digitised from Jagla (2004); arrow indicates direction of increasing maturity. Large open circles: Lava lake jointing patterns digitised from Peck and Minakami (1968), for Makaopuhi lava lake (ML) and Alae lava lake (AL). Filled circles: columnar jointing in silicic ignimbrite; data from Wright et al. (2011). Crosses are desiccation crack patterns in starch (digitised from Mueller 1998).

Fig. 9

Crystal size distributions for the Fingal's Cave lava flow (A, top) and for the lava lobe within the hyaloclastite unit (B, bottom). Both sets of samples give CSDs that are linear with a down-turn at low crystal size. See text for details. Dashed lines indicate entablature samples.

Fig. 10

Silicate liquid immiscibility in the hyaloclastite lava lobe. Top: back-scattered SEM image showing bright Fe-rich droplets immersed in a silicic (mid-grey) liquid. Droplets coalesce and adhere to plagioclase crystal margins. Tabular, euhedral plagioclase (pl, dark grey); cruciform/ dendritic oxides (ox, white); pyroxene (px, grey). Scale bar 25 μm. Bottom: Plane-polarised photomicrograph showing liquid immiscibility between plagioclase grains (centre). Dendritic oxides (black) and altered olivine/ pyroxene (brown) can also be seen. Scale bar 50 μm.

Fig. 11

Minor element concentrations (TiO_2, FeO and MgO) in plagioclase from Staffa as a function of Anorthite content (X_{An}). All elements show a break in slope which probably corresponds to crystallisation of new phases (Fe-Ti oxides and clinopyroxene) during plagioclase crystallisation.

Fig.12

The time to cool from emplacement temperature (~1170 °C) to 950 °C, estimated from crystal size distributions for the Fingal's Cave lava, with assumed crystal growth rates of 10^{-9} mm s^{-1} (circles) and 10^{-8} mm s^{-1} (squares). The solid line is a linear regression fit with equation $y = 1.18x + 35.8$, and the dashed line shows the approximate position of the flow top.

Table 1

Statistical data from natural and experimental jointing patterns. Also shown are statistical data calculated from previously published data: [1] from images in O'Reilly (1879); [2] Beard 1959; [3] Budkewitsch and Robin (1994); [4] from images in Peck and Minakami (1968); [5] from data of Wright et al. (2011); [6] Crain (1978); [7] Tanemura and Hasegawa (1980), reported in Budkewitsch and Robin (1994); [8] from images in Jagla (2004); [9] from images in Mueller (1998)

Table 2

Crystal size distributions for samples from the Fingal's cave flow, west coast traverse (locality 8) and the hyaloclastite lava lobe (locality 10).

FIGURES AND TABLES

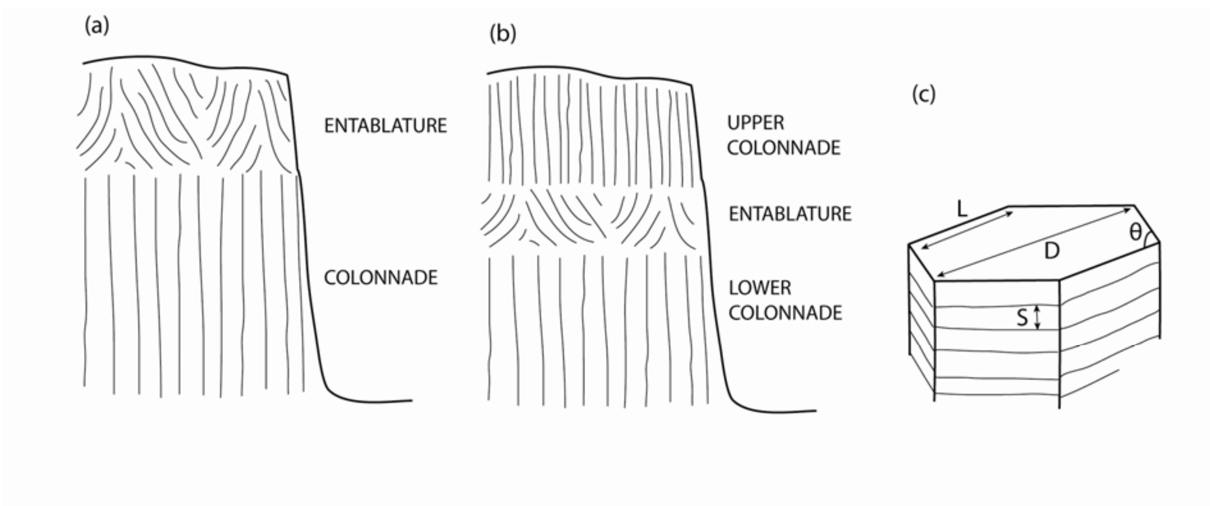

Figure 1

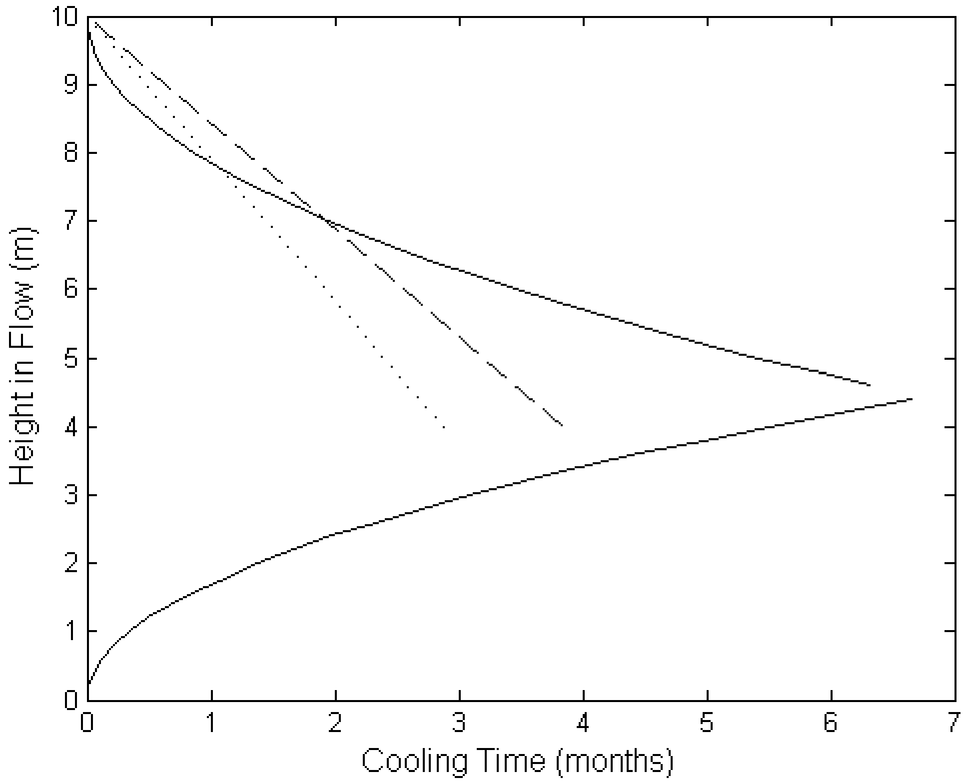

Figure 2

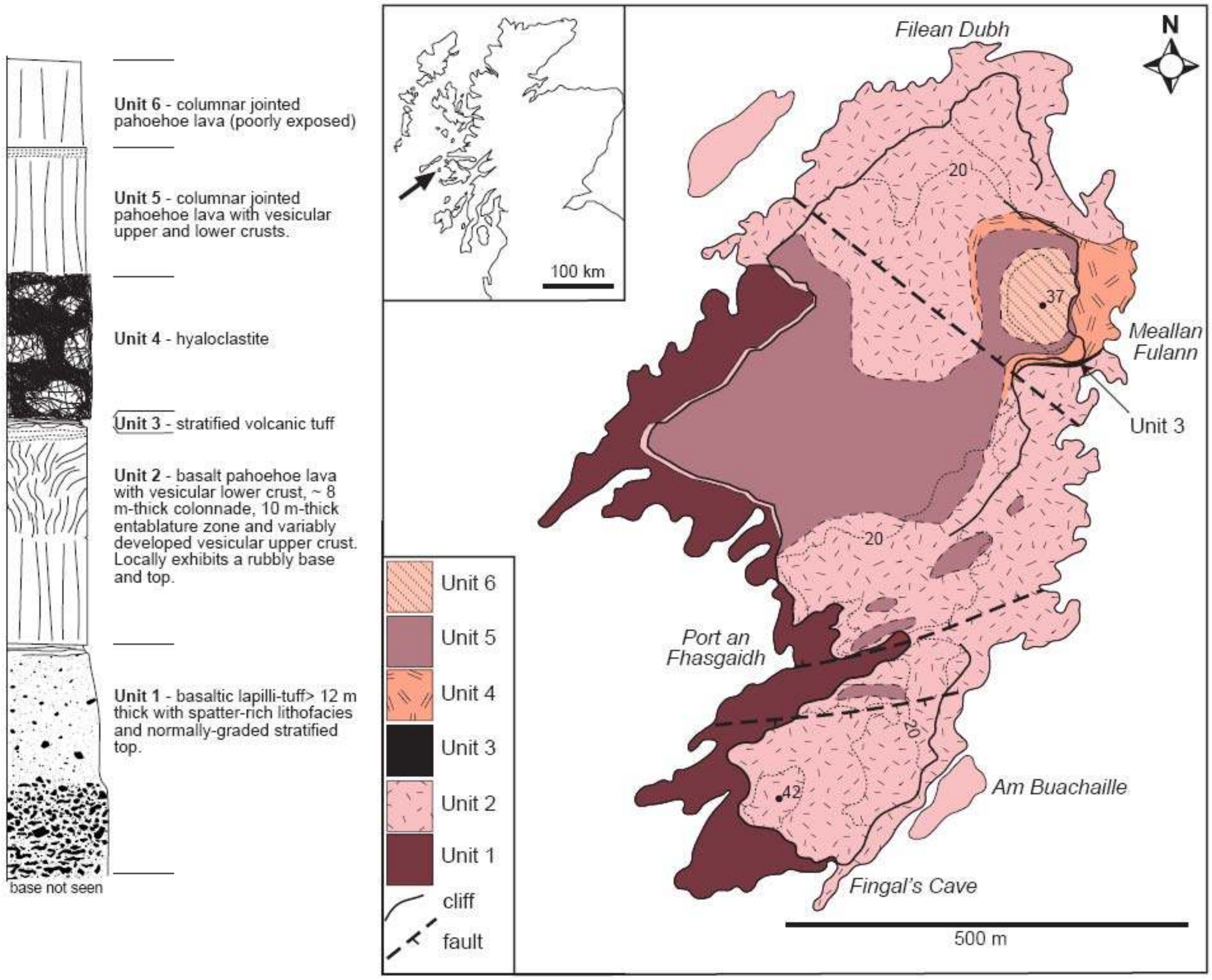

Unit 6 - columnar jointed pahoehoe lava (poorly exposed)
Unit 5 - columnar jointed pahoehoe lava with vesicular upper and lower crusts.
Unit 4 - hyaloclastite
Unit 3 - stratified volcanic tuff
Unit 2 - basalt pahoehoe lava with vesicular lower crust, ~ 8 m-thick colonnade, 10 m-thick entablature zone and variably developed vesicular upper crust. Locally exhibits a rubbly base and top.
Unit 1 - basaltic lapilli-tuff> 12 m thick with spatter-rich lithofacies and normally-graded stratified top.
base not seen
100 km
Filean Dubh
N
20
37
Meallan Fulann
Unit 3
20
Port an Fhasgaidh
20
42
Am Buachaille
Fingal's Cave
500 m
Unit 6
Unit 5
Unit 4
Unit 3
Unit 2
Unit 1
cliff
fault

Figure 3

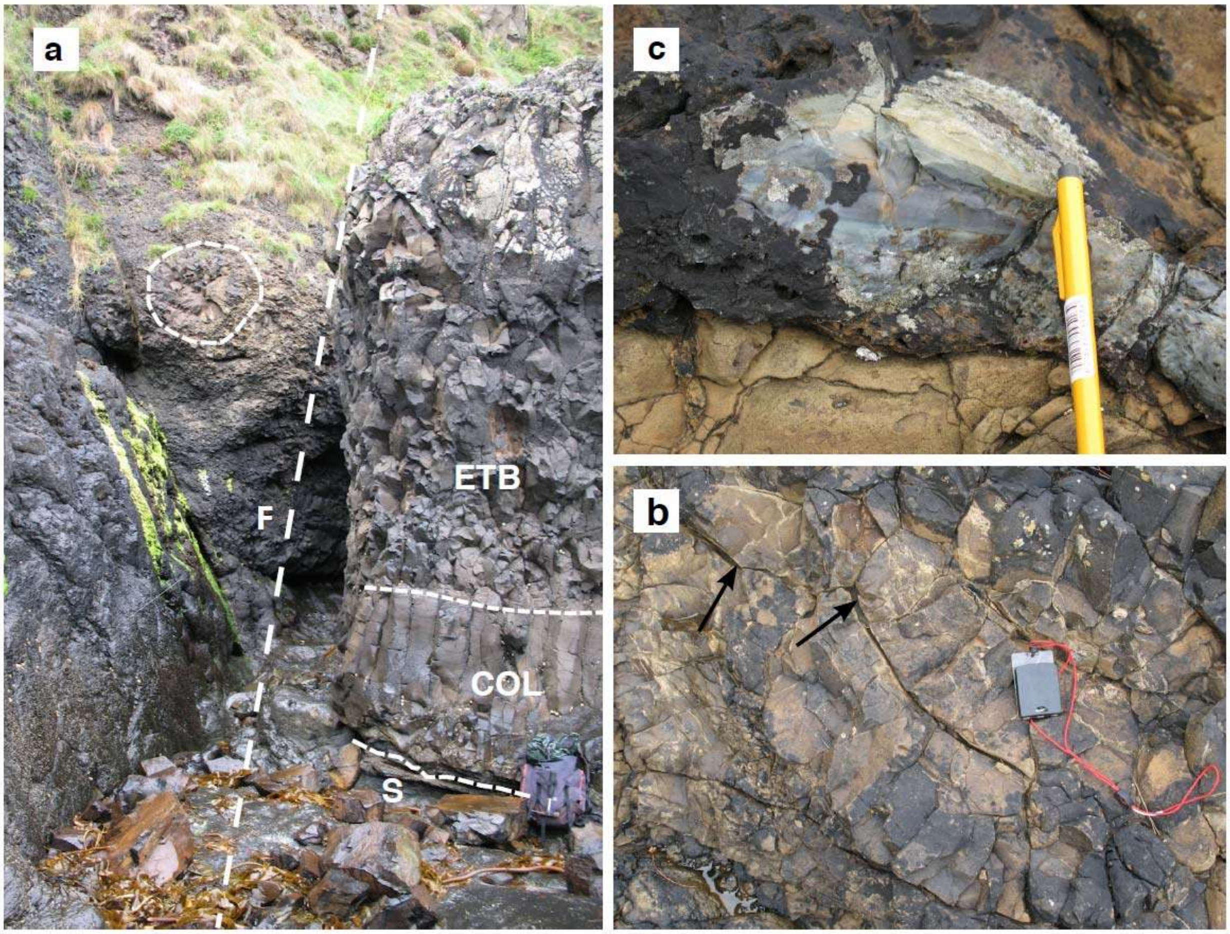

Figure 4

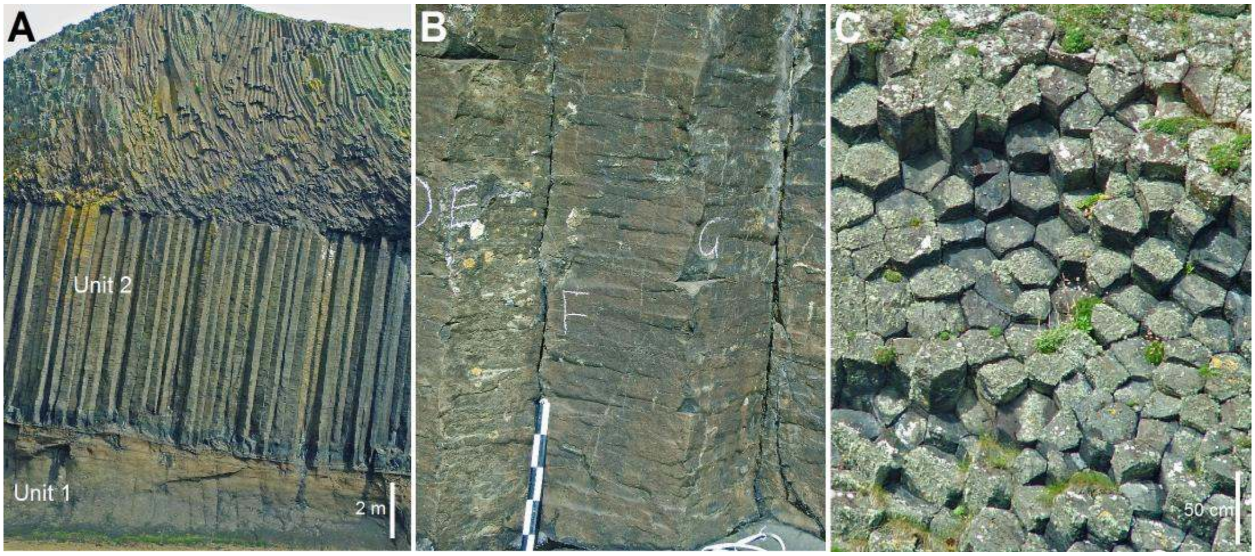

Figure 5

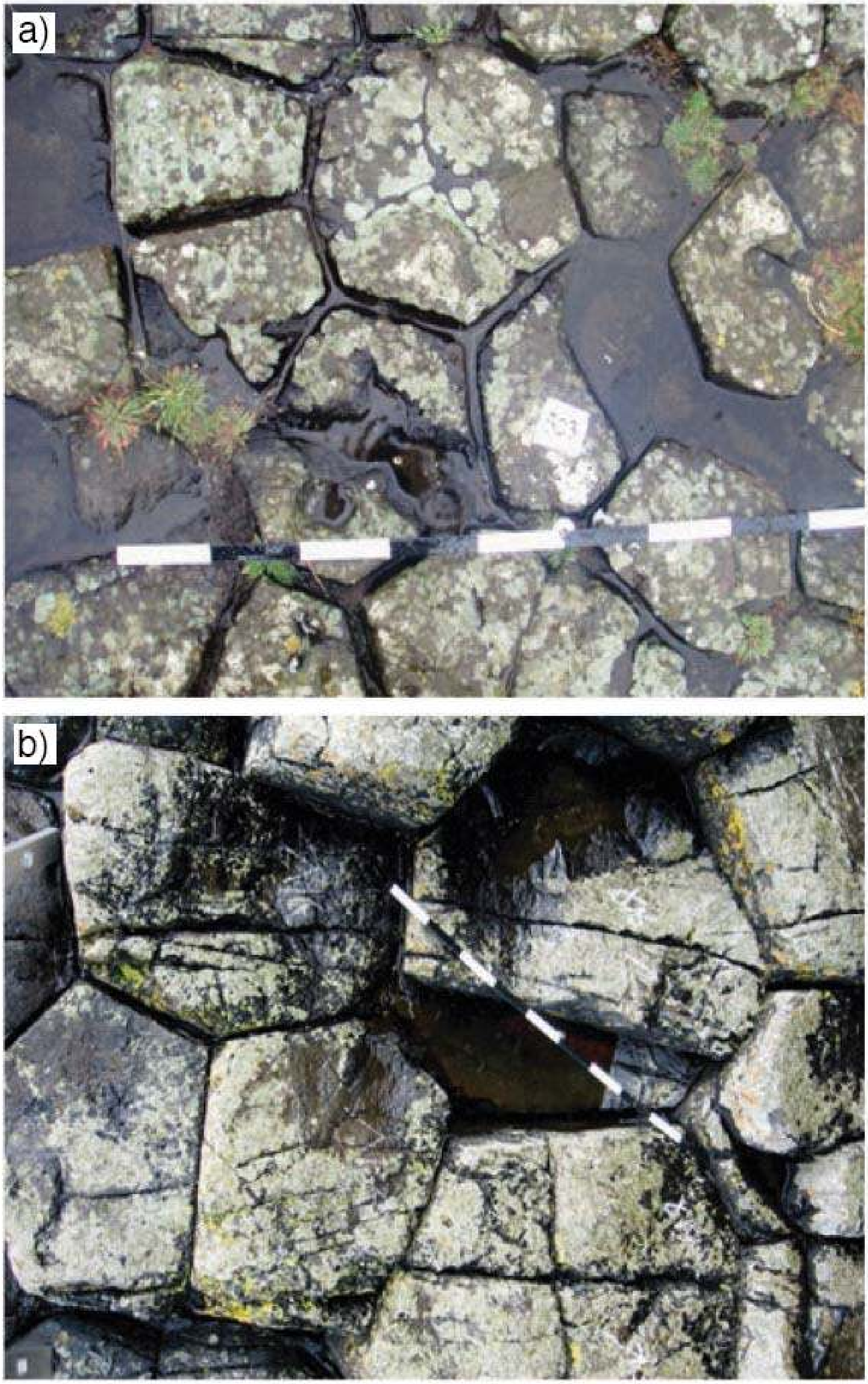

Figure 6

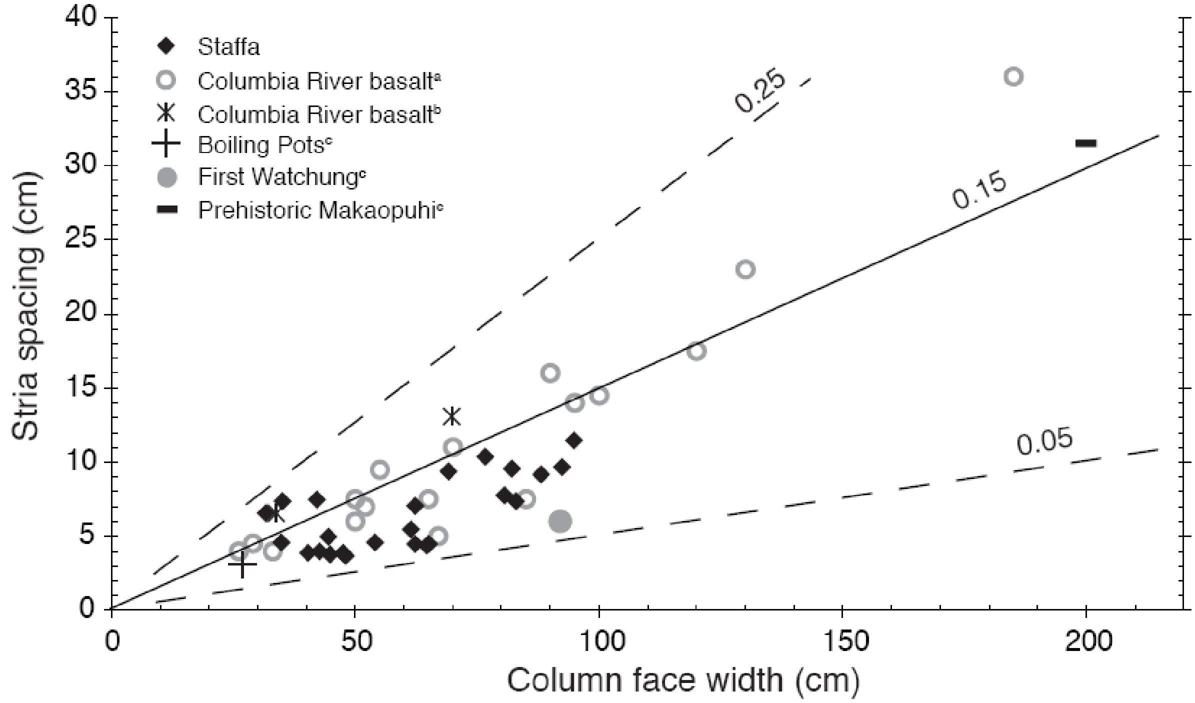
Staffa
Columbia River basalt[a]
Columbia River basalt[b]
Boiling Pots[c]
First Watchung[c]
Prehistoric Makaopuhi[c]
0.25
0.15
0.05
Stria spacing (cm)
Column face width (cm)
0
5
10
15
20
25
30
35
40
0
50
100
150
200

Figure 7

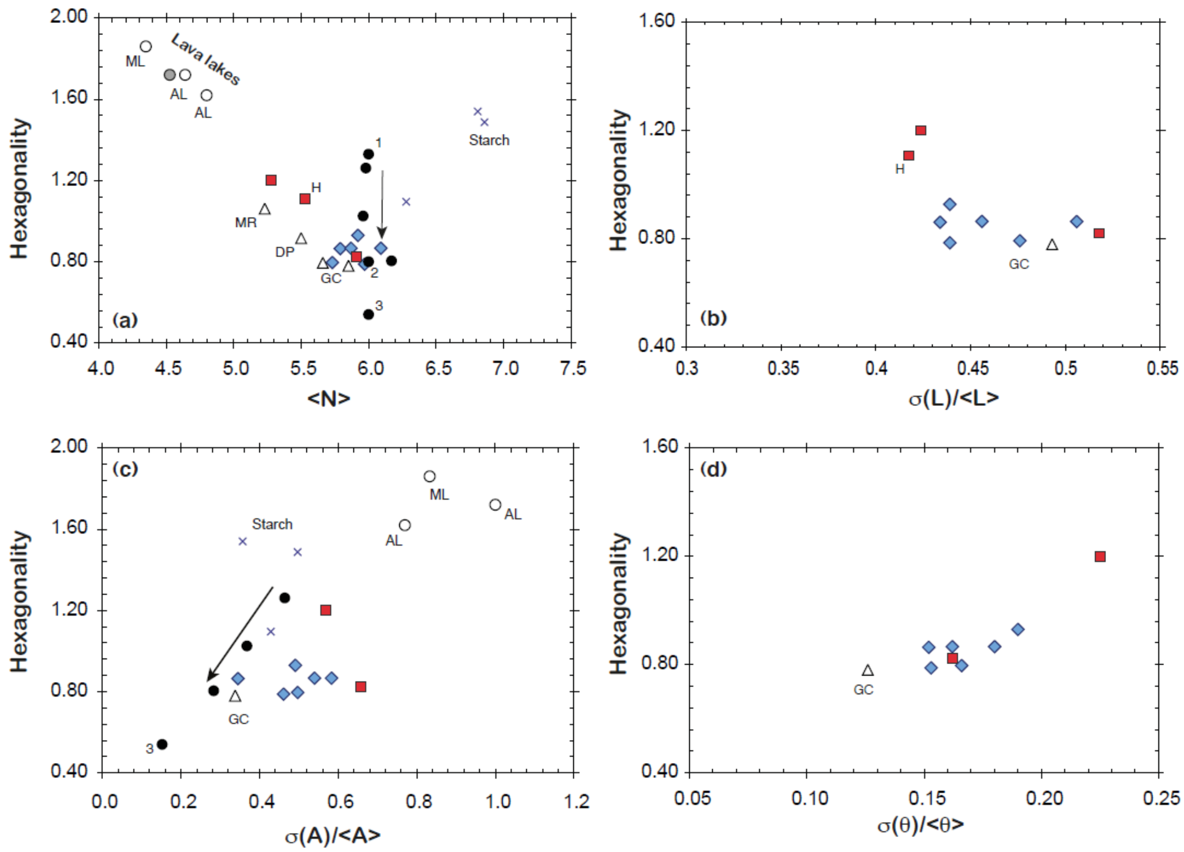
(a)
Hexagonality
<N>
Lava lakes
ML
AL
AL
Starch
H
MR
DP
GC
1
2
3
(b)
σ(L)/<L>
H
GC
(c)
σ(A)/<A>
Starch
ML
AL
AL
GC
3
(d)
σ(θ)/<θ>
GC

Figure 8

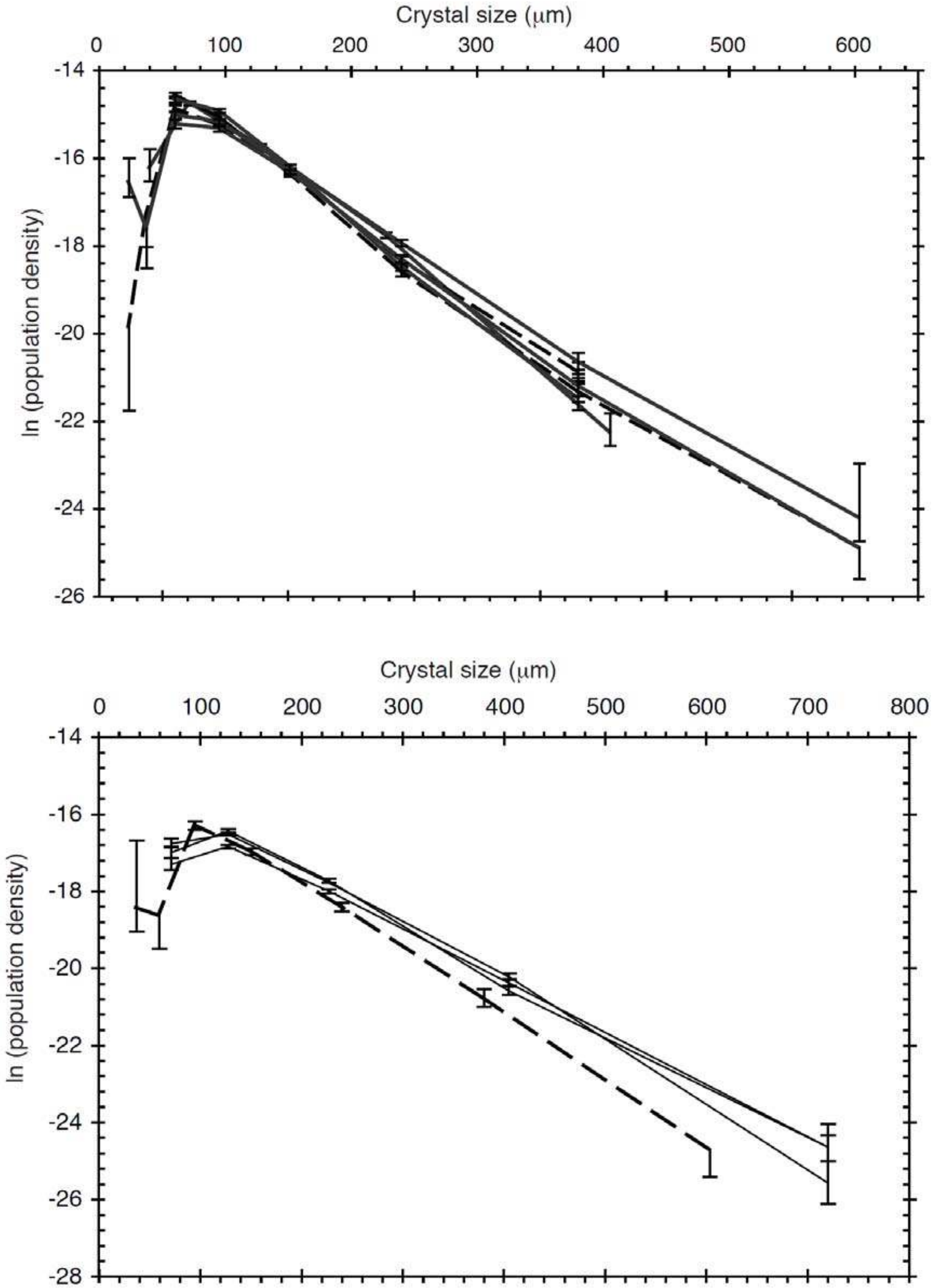
Crystal size (μm)
0
100
200
300
400
500
600
-14
-16
-18
-20
-22
-24
-26
ln (population density)
Crystal size (μm)
0
100
200
300
400
500
600
700
800
-14
-16
-18
-20
-22
-24
-26
-28
ln (population density)

Figure 9

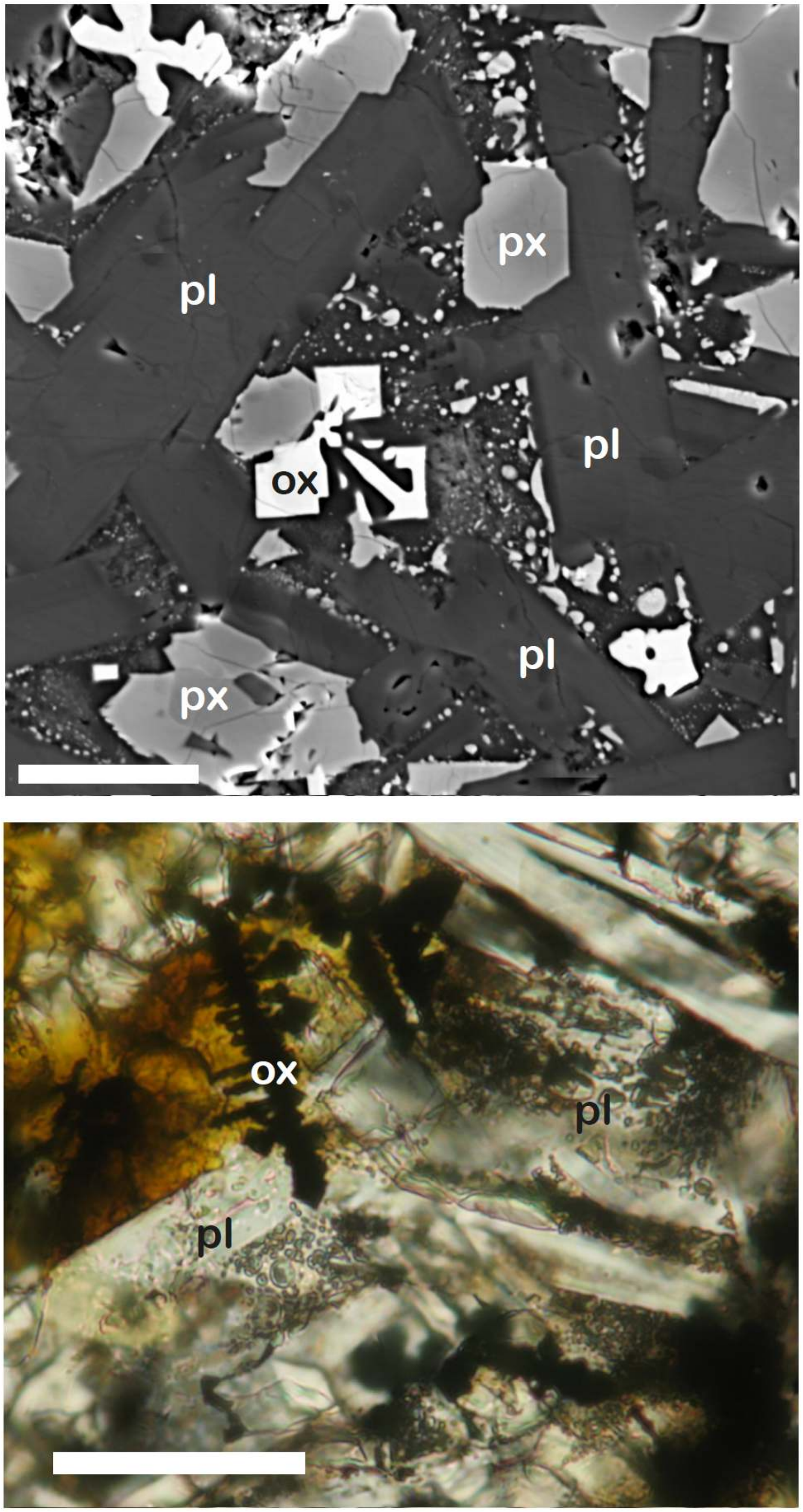

Figure 10

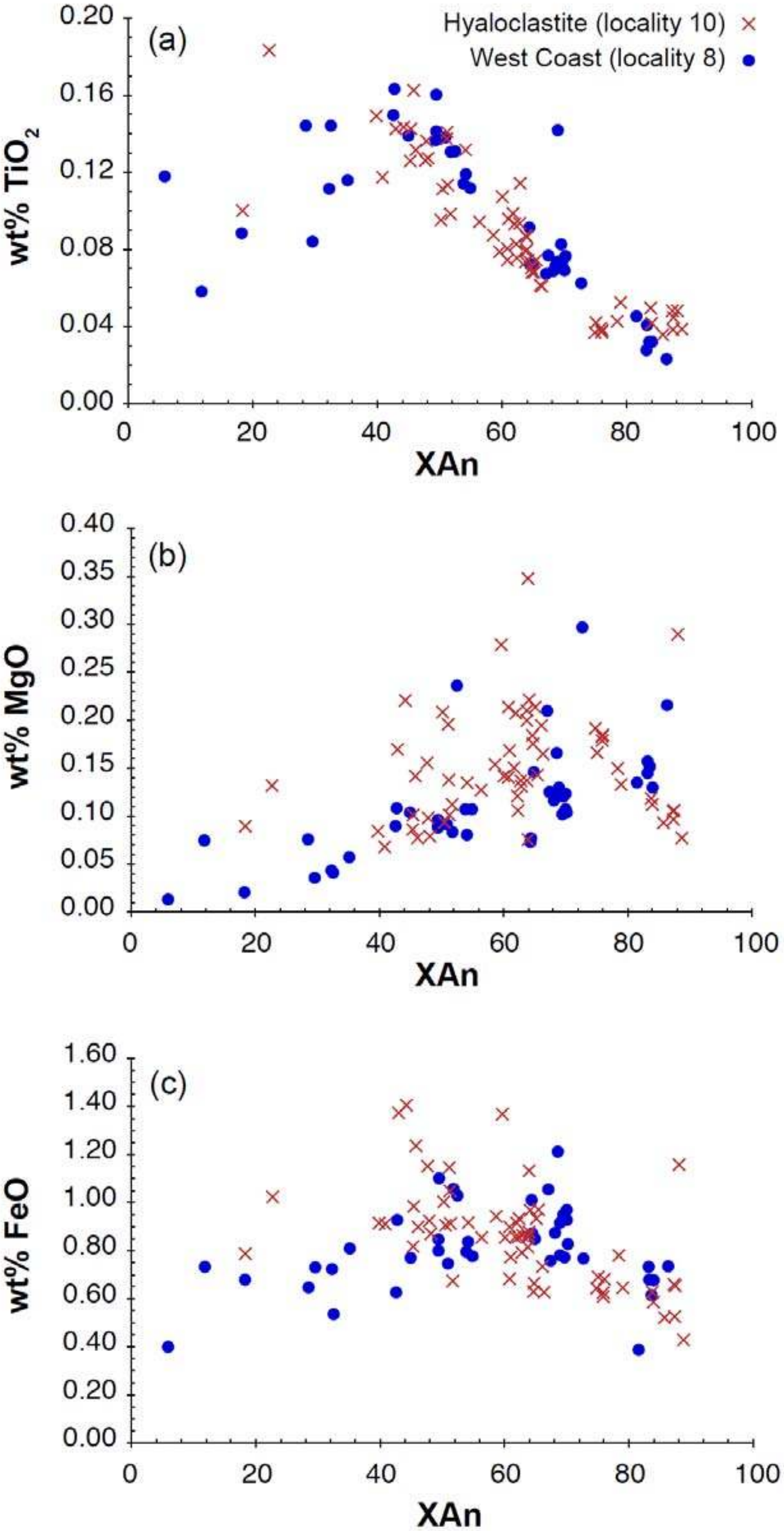

(a)
Hyaloclastite (locality 10)
West Coast (locality 8)
wt% TiO_2
0.20
0.16
0.12
0.08
0.04
0.00
0
20
40
60
80
100
XAn
(b)
wt% MgO
0.40
0.35
0.30
0.25
0.20
0.15
0.10
0.05
0.00
XAn
(c)
wt% FeO
1.60
1.40
1.20
1.00
0.80
0.60
0.40
0.20
0.00
XAn

Figure 11

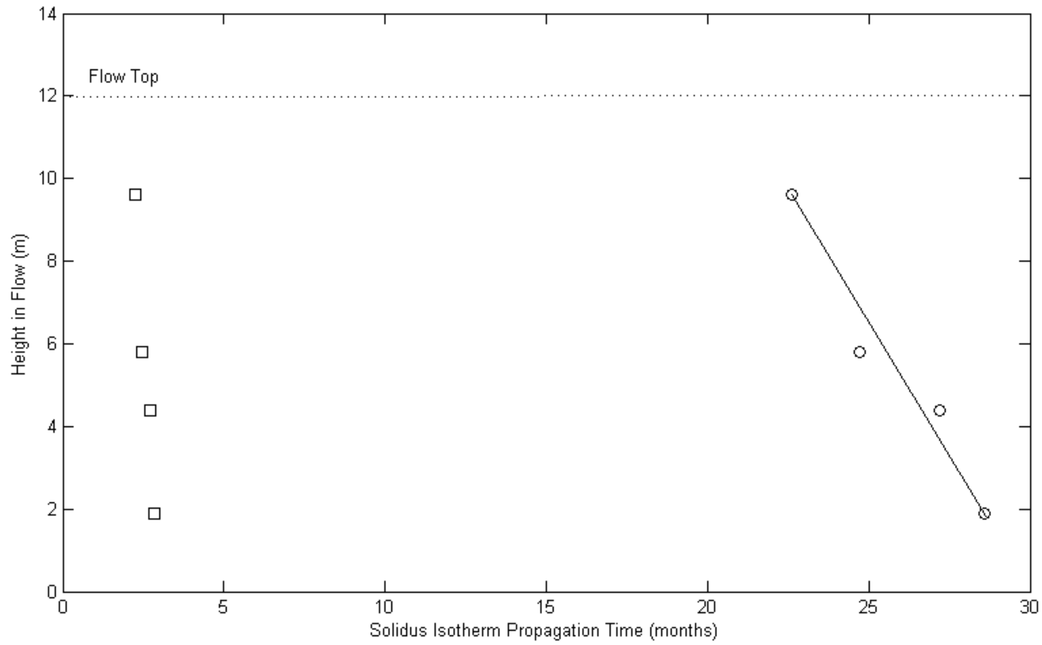
Flow Top
Height in Flow (m)
Solidus Isotherm Propagation Time (months)
0
2
4
6
8
10
12
14
0
5
10
15
20
25
30

Figure 2

	No. columns	Avg no. sides	χ_N	Mean column diameter (cm)	Mean side length $\langle L \rangle$ (cm)	$\sigma(L)$	$\sigma(L)/\langle L \rangle$	column top area $\langle A \rangle$ (cm^2)	$\sigma(A)$	$\sigma(A)/\langle A \rangle$	Mean internal angle °	$\sigma(\theta)$	$\sigma(\theta)/\langle \theta \rangle$
Locality 1 (colonnade)	71	5.7	0.80	77.5	38.3	18.2	0.476	3157	1571	0.497	117.8	19.5	0.166
Locality 2 (colonnade)	138	5.8	0.86	83.4	40.1	17.4	0.434	3709	1278	0.345	118.2	18	0.152
Locality 3 (colonnade)	53	5.9	0.93	91.8	41.8	18.3	0.439	4329	2124	0.491	118.9	22.6	0.190
Locality 5 (colonnade)	68	5.9	0.87	113.5	53.9	24.6	0.456	7520	4059	0.540	118.7	19.2	0.162
Locality 6 (colonnade)	100	6.1	0.87	74.6	33	16.7	0.506	2836	1654	0.583	120.7	21.8	0.180
Locality 8 (colonnade)	37	6.0	0.79	87.8	41.8	18.3	0.439	4326	1992	0.461	119.7	18.4	0.153
Locality 4 (entablature)	58	5.9	0.82	24.5	11.6	6.01	0.518	308.5	202.7	0.657	119.1	19.3	0.162
Locality 7 (entablature)	172	5.3	1.20	21.4	11.9	5.04	0.424	271.1	154.1	0.568	111.9	25.2	0.225
Locality 10 (hyaloclastite)	13	5.5	1.11		16.4	6.84	0.417						
Giant's Causeway [1]	76	5.9	0.78		27.7	13.7	0.493			0.338	119	13.7	0.126
Giant's Causeway [2]	400	5.7	0.80										
Devil's Postpile [3]	400	5.5	0.92										
Mount Rodeix, Auvergne [3]	200	5.2	1.06										
Alae lava lake [4]	26	4.8	1.62							0.77			
Alae lava lake [4]	72	4.6	1.72							1.0			
Makaopuhi lava lake [4]	55	4.4	1.86							0.833			
Paycuqui ignimbrite, Cerro Galan, Argentina [5]		4.5	1.72	75									
Poisson model [6]	46000	6.0	1.33										
Anti-clustered (random close-packing) model [7]	675	6.0	0.80										
Mature (regular close-packing) model [7]	500	6.0	0.54							0.152			
Numerical model, t = 10 [8]	110	6.0	1.26							0.464			
Numerical model, t = 20 [8]	99	6.0	1.03							0.368			
Numerical model, t = 280 [8]	93	6.2	0.80							0.283			
Starch, d = 7mm [9]	100	6.8	1.54							0.357			
Starch, d = 11mm [9]	100	6.3	1.10							0.429			
Starch, d = 19 mm [9]	100	6.9	1.49							0.497			

Table 1

	Locality 8				Locality 10					
	STA7	STA8	STA9	STA10	STA11	STA12	STA13	STA14	STA16	STA15
Facies	Lower colonnade	Lower colonnade	Lower colonnade	Entablature	Lower colonnade	Lower colonnade	Lower colonnade	Entablature	Entablature	Upper colonnade
Height above base (cm):	33	280	420	800	70	135	180	240	275	380
Total area measured (mm^2)	3.86	3.88	3.88	1.49	1.81	1.81	1.51	1.81	1.81	1.81
No. crystals measured	1114	1464	1465	431	1143	1396	1510	1278	1390	1464
CSD gradient = -1/Gt	-0.0133	-0.014	-0.0154	-0.0168	-0.0205	-0.0191	-0.0238	-0.0193	-0.0233	-0.0198
±	0.0002	0.0005	0.0007	0.0007	0.0006	0.0005	0.0006	0.0005	0.0006	0.0005
ln (population density)	-15.07	-14.70	-14.35	-14.53	-13.32	-13.35	-12.64	-13.5	-12.85	-13.26
±	0.08	0.07	0.07	0.14	0.1	0.08	0.09	0.07	0.09	0.07
Crystallisation rate (mm/s)	1.0E-09	1.0E-09	1.0E-09	1.0E-09	5.0E-08	5.0E-08	5.0E-08	5.0E-08	5.0E-08	5.0E-08
Residence time t (day)	870	827	752	689	11	12	10	12	10	11.7

Table 2